J. Fluid Mech. (1994), *vol.* 278, *pp.* 201–228

Potential energy in steep and breaking waves

By WILLIAM W. SCHULTZ[1], JIN HUH[1]† AND OWEN M. GRIFFIN[2]

[1]Department of Mechanical Engineering and Applied Mechanics, University of Michigan, Ann Arbor, Michigan 48109–2125, USA

[2]Remote Sensing Division, Naval Research Laboratory, Washington, DC 20375–5000, USA

(Received 9 April 1993 and in revised form 19 April 1994)

We find that the RMS wave height (square root of the potential energy) rather than peak-to-peak wave height is a better experimental and analytic criterion for determining when a regular, two-dimensional deep-water wave will break. A spectral algorithm for two-dimensional potential flow is developed and used to compare breaking onset criteria for energy input from (i) converging sidewalls, (ii) a submerged disturbance, and (iii) wave focusing. We also find that wave-breaking criteria (potential energy or the more classical peak-to-peak wave height) are a function of the rate of energy input. Large plunging waves occur when energy input rates are large. As energy input rates become smaller there is a smooth transition to smaller spilling waves. The various energy input methods show similar breaking trends in the limit as the energy input rate becomes small – waves break when the potential energy becomes approximately 52 % of the energy for the most energetic Stokes wave, with the formation of a singularity immediately before the crest. The effects of wave modulation and reflection are briefly discussed and shown not to affect the potential energy breaking criterion significantly. The experimental scatter of the RMS wave height is shown to be half that of wave steepness during incipient breaking in wave packets.

1. Introduction

The ocean wave energy spectra and the surface hydrodynamics of ship wakes are strongly affected by breaking waves, especially at the bow and in the near wake. Breaking waves are usually classified into two types: plunging breakers (with a large degree of overturning) and spilling breakers (with white water only near the crest). Plunging breakers are an important factor in the overturning of ships in rough seas, and they often form continuously at the bow of a ship, producing bubbles and foam that strongly affect the signature of a ship wake. Spilling breakers are more common in the open ocean (owing to wind) and in breaking wave experiments; they also occur in the near-ship Kelvin wave pattern.

A recent discussion of ship wake hydrodynamics and the related remote sensing issues is given by Reed *et al.* (1991), and extensive summaries of breaking wave experiments are available (Rapp & Melville 1990; Bonmarin 1989; Kjeldsen & Myrhaug 1978). While the mechanisms for plunging and spilling breaking waves are often thought to be quite different, we will show that their formation is similar with their qualitative features depending mainly on the energy input rate.

† Present address: Korea Atomic Energy Institute, Taejon, Korea

The fundamental experiments for determining two-dimensional wave-breaking criteria (apart from that induced by wind–wave interaction) fall into three main categories: (i) the focusing of essentially two-dimensional waves in the lateral direction (Ramberg & Griffin 1987; Van Dorn & Pazan 1975); (ii) the towing of a submerged object such as a hydrofoil to produce steady breakers (Duncan 1981, 1983); and (iii) the focusing of variable-length waves from a modulated wavemaker or wave source to produce unsteady breakers (Dommermuth *et al.* 1988; Duncan, Wallendorf & Johnson 1987; Rapp & Melville 1990) or the overturning of an irregular wave train (Ochi & Tsai 1983) to produce unsteady breakers.

The most comprehensive laboratory study of unsteady deep-water breaking is that of Rapp & Melville (1990). The dispersive character of deep-water waves was used to focus a wave packet to generate a single unsteady breaking event at a controlled location in the wave channel. Rapp & Melville found that the growth rate of the waves prior to breaking was an important factor in predicting breaking. This had been found previously by Van Dorn & Pazan (1975) and to a lesser extent by Ramberg, Barber & Griffin (1985) in their convergent channel experiments. A recent review by Banner & Peregrine (1993) is more descriptive in nature and does not attempt to develop a wave-breaking criterion.

Several of these experimental studies propose a wave-breaking criterion based on peak-to-peak (crest-to-trough) wave height. However, the validity of a standard criterion has been questioned (Melville & Rapp 1988), in part because peak-to-peak wave heights vary significantly during breaking and often decrease just before breaking. Clearly, no breaking criteria can be simple and precise. We have opted for a simple one in hopes that it can be more universally applied, although experimentally or computationally determined criteria will be a function of many parameters. Extensive discussions of breaking criteria based on wave height are given in Ochi & Tsai (1983), Huang *et al.* (1986), and Bonmarin (1989). Breaking criteria based on crest acceleration are discussed by Srokosz (1986) and Longuet-Higgins (1985). Experimental determination of the onset of breaking is also difficult without detailed velocity measurements at the crest (Melville & Rapp 1988; Van Dorn & Pazan 1975), which are usually not available and are difficult to obtain.

Computational studies of breaking waves usually form waves by applying a point pressure disturbance (Longuet-Higgins & Cokelet 1976) or obtain breaking conditions simply from having sufficiently energetic initial conditions (Vinje & Brevig 1981). While many algorithms have been developed that simulate breaking waves, no study has systematically examined the parameters to determine breaking criteria. For example, wave breaking caused by a modulated wavemaker has been verified computationally by Dommermuth *et al.* (1988), but these computations were so expensive that only one experimental event was verified. In addition, previous computations tend to show plunging waves instead of the more commonly observed spilling breakers.

In this study, we computationally examine the steepening and breaking of deep water waves generated by the experimental methods cited above. We consider only spatially periodic computations, so an *ad hoc* energy input term is deduced for the convergent wave channel. Although the periodic boundary conditions preclude studying the wavemaker problem, we briefly examine the effect of wave modulation using a larger computational region (more than one primary wavelength) as in Dold & Peregrine (1986). The effect of beach reflections can be modelled by putting a small standing wave component in the initial conditions. Finally, to crudely model waves

produced by submerged hydrofoils we use an array of simple submerged dipoles. The array is used to preserve spatial periodicity.

There are difficulties in interpreting the differences caused by the computational spatial periodicity as compared to temporal periodicity in most experiments. These differences also affect comparisons of temporal *vs.* spatial growth when we model a convergent channel. Also, experiments continue after breaking occurs, while the time-marching computations must stop at the first occurrence of breaking unless an *ad hoc* condition models the turbulence and air entrainment. We will show that accurate spectral computations break down sooner, indicating the possible formation of a singularity and evidence of the failure of potential theory before the wave crest approaches the forward face.

Only wave height experimental data are analysed here since these traditional measurements are easily obtained compared to velocity measurements. These data are used to show that potential energy reduces the experimental scatter in breaking criteria and to show that it acts as a better *predictor* (rather than just indicator) of breaking.

In § 2, we pose the problem for periodic waves, including the modelling of the growth in energy and the effect of submerged disturbances. Section 3 contains a summary of earlier computational progress followed by a formulation of the two computational techniques used in this study. Section 4 presents numerical results, including comparisons to related computational schemes and the development of breaking criteria as a function of the energy input rate. The computations are compared to some previous experiments in § 5, and § 6 summarizes the findings.

2. Problem formulation

The problem domain is shown in figure 1(*a*). The scales are chosen to make gravity, density, and the primary wavenumber unity. The phase speed and angular velocity of a linear wave will then be unity as well. The initial boundary value problem solution is described by a complex potential $w(\xi) = \phi + \mathrm{i}\psi$, where ϕ is the velocity potential, ψ is the stream function and $\xi = x + \mathrm{i}y$ represents the two spatial coordinates. At every time step, the unknown boundary values of the velocity potential (half of the values are known from the boundary conditions) are solved using the Cauchy integral theorem:

$$\oint_{\partial\Omega} \frac{w(\xi)}{\xi - \zeta_k} \mathrm{d}\xi = \mathrm{i}\alpha w(\zeta_k)\,, \tag{2.1}$$

where α is 0 or 2π if the location of the kernel singularity, ζ_k, is outside or inside the boundary, respectively. If the kernel singularity is on the boundary ($\zeta_k \in \partial\Omega$), α is equal to the included angle, and the integral is treated as principal-valued.

The kinematic and dynamic boundary conditions of a free surface for inviscid flow are given as

$$\frac{\mathrm{D}\xi}{\mathrm{D}t} = \frac{\mathrm{d}w^*}{\mathrm{d}\xi} \tag{2.2}$$

and

$$\frac{\mathrm{D}\phi}{\mathrm{D}t} = -y + \frac{1}{2}\left|\frac{\mathrm{d}w^*}{\mathrm{d}\xi}\right|^2 - p. \tag{2.3}$$

Here, p is a prescribed pressure (normally 0, as in this study, unless surface tension or wind effects are included), $\mathrm{D}/\mathrm{D}t$ is a material derivative, and * denotes the complex

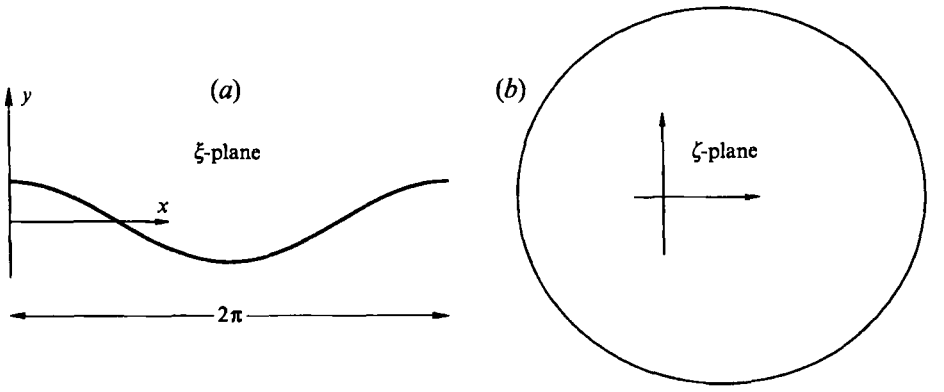

FIGURE 1. Problem domain: (*a*) physical space, (*b*) mapped space.

conjugate. The kinematic condition requires that material particles on the free surface stay on the free surface, and the dynamic boundary condition requires that the pressure remains constant at the free surface in the absence of surface tension.

We complete the problem formulation by applying a periodic boundary condition in the horizontal direction such that $w(\xi) = w(\xi + 2\pi)$, the deep-water condition requiring $w \to 0$ as $y \to -\infty$, and initial conditions. These initial conditions on the free surface can be homogeneous if the waves are forced by submerged dipoles. For purposes of illustration and comparison, we generally use the same free-surface initial conditions as McIver & Peregrine (1981):

$$y = a\sin x \quad \text{and} \quad \phi = a\cos x. \tag{2.4}$$

These initial conditions satisfy linear theory as the wave amplitude a becomes small. We apply increasing values of a until the wave breaks. We also apply more complicated initial conditions to examine wave modulation and the effect of applying initial conditions computed from steadily progressing waveforms using the method of Schwartz & Vanden-Broeck (1979).

Finally, we note that the above formulation is ill-posed in the sense that the solution to the complex potential w is non-unique. A constant imaginary number can be added to the solution. An extra constraint must be added if a standard direct solver is used.

2.1. *Modelling the convergent wave channel*

The convergent channel is inherently a three-dimensional problem. If the convergence is small in z (the spanwise direction out of the plane of figure 1*a*), a multiple-scales approach will lead to the three-dimensional effect being delayed to a Poisson equation at higher order, with the lowest-order solution being that of a non-convergent wave channel. The sidewall boundary condition simply becomes $\phi_z = \eta\phi_x$, where η is the slope of the converging walls and the subscripts x and z represent partial differentiation. This method of analysis precludes the possibility of modelling the flow as spatially periodic and hence makes the problem intractable using periodic algorithms.

All these modifications would add *considerable* computational complexities. Instead we simply add a term in the Bernoulli equation that causes the energy to increase

exponentially in time so that (2.3) becomes

$$\frac{\mathrm{D}\phi}{\mathrm{D}t} = -y + \frac{1}{2}\left|\frac{\mathrm{d}w^*}{\mathrm{d}\xi}\right|^2 + \gamma\phi. \tag{2.5}$$

This *ad hoc* term is similar (but with the opposite sign) to the dissipative term used to develop radiation conditions. Starting with a wave of small amplitude, this term eventually causes the wave to break, much like the convergent channel. While this causes exponential temporal growth in the computations, the experimental energy per unit width, E, grows in space. The corresponding temporal growth parameter can be approximately related through the group velocity and conservation of energy by

$$\gamma = \frac{1}{E}\frac{\mathrm{d}E}{\mathrm{d}t} = -\frac{1}{z_w}\frac{\mathrm{d}z_w}{\mathrm{d}t} = -\frac{1}{z_w}\frac{\mathrm{d}z_w}{\mathrm{d}x}c_g = \frac{\eta c_g}{z_w}. \tag{2.6}$$

The dimensionless values for the experiments considered here ($\eta = 1/16$) correspond to

$$\gamma = K\frac{T^2}{W}, \tag{2.7}$$

where the dimensional constant K is 0.008 m s^{-2}, and W and T are the dimensional values of the local channel width and wavemaker period, respectively. The small value of K keeps the growth parameter below 0.05 in the region of breaking.

2.2. *Modelling periodic submerged disturbances*

We also wish to show how submerged disturbances can force wave breaking. Retaining the periodic boundary condition requires that the disturbances be periodic. Rather than model a complex two-dimensional shape such as a hydrofoil, we use a periodic array of moving dipoles:

$$w_{dp} = a_{dp}\cot\left[\tfrac{1}{2}(\xi - \xi_{dp})\right], \tag{2.8}$$

where a_{dp} and ξ_{dp} are the strength and location of the dipole, respectively. The dipole depth, d_{dp}, and velocity, v_{dp}, are prescribed such that $\xi_{dp} = (2\pi + v_{dp}t, -d_{dp})$. As long as the strength of the dipole is not too large and the depth is not too small, the dipole can closely represent a cylinder of radius r_{dp} if $a_{dp} = v_{dp}r_{dp}^2/2$. Previous wave computations in three dimensions have shown good agreement between dipoles and complex bodies (which are more difficult to compute) if the disturbance is sufficiently deep (Cao, Schultz & Beck 1990).

Since the dipole is a simple pole in the complex potential plane, the only alteration required is to subtract the singular part of the solution and solve only for the remaining regular term from the integral equation (2.1).

3. Computations of steep and breaking waves

3.1. *Recent computational advances*

Although formal analytical techniques have been developed for small-amplitude gravity waves, unsteady and steep waves must be solved numerically. The most efficient of these algorithms are based on boundary integral techniques. Even then, the algorithms can be time consuming. Hence, no thorough and complete parametric study has been performed on gravity waves. Usually, to reduce the computational

effort, the problem domain is kept as small as possible by applying periodic boundary conditions. We have adopted this restriction here. Recently, computations with many fundamental wavelengths inside the periodic domain have been applied by Dold & Peregrine (1986), and the non-periodic fully nonlinear wavemaker problem has been computed by Dommermuth *et al.* (1988). Casual observations of breaking waves show that they are not spatially periodic. Here we only present results for the periodic problem, although by using a large spatial period, the model can approximate results on an infinite domain.

The boundary integral numerical schemes for irrotational flow problems can be divided into three general approaches based on Green's functions (Longuet-Higgins & Cokelet 1976; Vanden-Broeck 1980), vortex dynamics (Baker, Meiron & Orszag 1982), or the Cauchy integral theorem for complex potentials (Vinje & Brevig 1981). To some extent, the three techniques give equivalent results (McIver & Peregrine 1981). Work by Dold & Peregrine (1984) has shown that algorithms based on the Cauchy integral theorem can be up to 50 times faster than Green's function algorithms and 10 times faster than those using vortex methods. Lin, Newman & Yue (1985) use the Cauchy formulation when solving two-dimensional problems and revert to the Green's function algorithm for axisymmetric problems. The efficiency of the complex algebra is significant.

Here we report on two algorithms based on the Cauchy integral theorem. The first is an improvement of a piecewise-linear algorithm of Vinje & Brevig (1981) as described in Schultz & Hong (1989). The second is a spectral technique similar to that proposed by Roberts (1983) and described in Huh (1991). We describe both methods because the first method, although less accurate and more computationally intensive, is also more robust. Comparisons will be presented.

In both methods, the physical domain is mapped to an approximate unit circle using the conformal transformation:

$$\zeta = e^{iz} \tag{3.1}$$

(see figure 1*b*). This eliminates the periodic boundary conditions and sharp computational corners used by Vinje & Brevig (1981). All derivatives are taken in the conformed space – the piecewise-linear method uses three-point central differences while the spectral method takes derivatives in the spectral space of the conformed representation. An alternative method (not used here) does not use conformal mapping but replaces the infinite periodic integrand with summation over a finite domain to form a cotangent kernel (Baker *et al.* 1982).

The algebraic system that results from discretizing the integral equation is iteratively solved for both methods using a generalized minimum residual method (GMRES) based on Saad & Schultz (1986). This variation of the conjugate gradient method for nonsymmetric matrices works well on the diagonally – dominant matrices of either method—especially matrices from the spectral algorithm.

Time marching is also similar in both algorithms. Fourth-order Runge–Kutta–Gill and predictor-corrector methods with an automatic adjustment of step size were both used, with the predictor-corrector method showing better computational efficiency, especially for the higher-accuracy computations. Ultimately, we decided on the use of the LSODA package from Lawrence Livermore to march in time.

3.2. *Piecewise-linear computational technique*

We take ζ_k in (2.1) to approach the boundary from the outside of the domain so that α is zero, although there are computational reasons for placing ζ_k slightly away

from the contour for some cases (Schultz & Hong 1989). The algebraic system is formed by discretization of (2.1), as explained in Vinje & Brevig (1981), and by letting the kernel singularity approach each of the N nodal points, i.e. $\zeta_k \to \xi_k$. A special limiting process is needed to evaluate the integration near ζ_k. The system of linear algebraic equations when w is discretized as a piecewise-linear function between the N boundary nodes is

$$\sum_{j=1}^{N} w_j \Gamma_{jk} = 0, \qquad k = 1, \ldots, N, \tag{3.2}$$

where

$$\Gamma_{jk} = \frac{\xi_{j+1} - \zeta_k}{\xi_{j+1} - \xi_j} \ln\left(\frac{\xi_{j+1} - \zeta_k}{\xi_j - \zeta_k}\right) - \frac{\xi_{j-1} - \zeta_k}{\xi_j - \xi_{j-1}} \ln\left(\frac{\xi_j - \zeta_k}{\xi_{j-1} - \zeta_k}\right), \quad j \neq k, \tag{3.3a}$$

$$\Gamma_{kk} = \ln\left(\frac{\xi_{k+1} - \xi_k}{\xi_{k-1} - \xi_k}\right). \tag{3.3b}$$

Equation (3.3) is evaluated using l'Hopital's rule when $j = k+1$ or $j = k-1$. Moving the known boundary conditions to the right-hand side gives a complex algebraic system for unknown ψ_j on the free surface.

When the complex potential is known along the domain boundary, the solution can be stepped forward in time using the Bernoulli equation and the kinematic boundary conditions. We solve this problem in a way similar to Vinje & Brevig (1981) but with the following changes:

(i) Rather than using the real or imaginary parts of the discretized Cauchy integral theorem (depending on whether the real or imaginary part of w is known), we use both to give $2N$ real equations and N real unknowns. Numerical experiments for known test cases (Schultz & Hong 1989) show that the least-squares solution is better for nearly circular contours, especially when the node placement is irregular (as will be the case after nodes are convected on the free surface). However, both results are second-order convergent. The solution time for a direct method of inverting the overdetermined system would be twice that of the determined system, but our experience with iterative conjugate gradient solvers indicates an increase in computational costs of only 10 %.

(ii) We use a conformal map to eliminate the bottom and periodic boundary conditions.

(iii) We use a central difference form for $\mathrm{d}w/\mathrm{d}\xi$ (or $\mathrm{d}w/\mathrm{d}\zeta$), while Vinje & Brevig (1981) use a truncated analytic form. Since the solution is piecewise-linear rather than analytic, we have found that some numerical instabilities can develop using the truncated analytic form. One can easily find examples where the derivative $\mathrm{d}w/\mathrm{d}\xi$ at a corner of the contour computed using the analytic form lies outside the range computed by the forward and backward derivatives. This violates the spirit of using piecewise-linear functions and can lead to numerical instabilities, although the truncated analytic form works better when the contour is smooth.

3.3. *Spectral computational technique*

Roberts (1983) used a desingularized kernel in his vortex formulation. Generally, it is difficult to find a suitable desingularized form of a kernel in an integral equation, but in the complex formulation it is relatively simple. The Cauchy integral equation

(2.1) can easily be rewritten as

$$\int \frac{w(s)-w(\zeta_k)}{\xi(s)-\zeta_k}\frac{\mathrm{d}\xi}{\mathrm{d}s}\mathrm{d}s = 0\,, \tag{3.4}$$

where the principal value integral can be replaced by the closed contour integral since the integrand is no longer singular. When ξ approaches ζ_k, the integrand approaches $\mathrm{d}w/\mathrm{d}s$ at the kth node point. Therefore, this kernel does not show the singular behaviour as ξ approaches ζ_k. The integral equation (2.1) is converted to the following sets of equations for $k = 1 \ldots N$:

$$\sum_{j=1}^{N} I_{jk} = 0 \qquad \text{for } k = 1,\ldots,N\,, \tag{3.5}$$

where N is the number of nodes, and I_{jk} is represented by

$$I_{jk} = \begin{cases} \dfrac{w_j - w_k}{\xi_j - \xi_k}\left(\dfrac{\mathrm{d}\xi}{\mathrm{d}s}\right)_j, & j \neq k \\ \left(\dfrac{\mathrm{d}w}{\mathrm{d}s}\right)_k, & j = k\,. \end{cases} \tag{3.6}$$

The algebraic system (3.5) effectively becomes a differential system because I_{jk} includes the derivative of w. To evaluate these derivatives spectrally, we use a cardinal function representation of w (Boyd 1989):

$$w(s) = \sum_{j=1}^{N} C_j(s) w_j, \tag{3.7}$$

where

$$C_j = \frac{1}{N}\sin\pi(s-s_j)\cot\frac{\pi}{N}(s-s_j), \tag{3.8}$$

and the derivative of C_j is

$$\frac{\mathrm{d}C_j}{\mathrm{d}s}(s_i) = \begin{cases} \dfrac{\pi}{N}(-1)^{i+j}\cot\dfrac{\pi}{N}(s_i - s_j), & i \neq j \\ 0, & i = j\,. \end{cases} \tag{3.9}$$

Then, (15) becomes

$$\sum_{j=1}^{N} \Gamma_{jk} w_j = 0 \qquad \text{for } k = 1,\ldots,N\,, \tag{3.10}$$

where the influence coefficients Γ_{jk} are now

$$\Gamma_{jk} = \begin{cases} \dfrac{1}{\xi_j - \xi_k}\left(\dfrac{\mathrm{d}\xi}{\mathrm{d}s}\right)_j + \dfrac{\mathrm{d}C_j}{\mathrm{d}s}(s_k), & j \neq k \\ -\displaystyle\sum_{i=1, i\neq k}^{N} \frac{1}{\xi_i - \xi_k}\left(\frac{\mathrm{d}\xi}{\mathrm{d}s}\right)_i, & j = k\,. \end{cases} \tag{3.11}$$

Unlike the method of Baker *et al.* (1982), which evaluates the integrand at every other point, the desingularized kernel is evaluated at every nodal point; hence, the matrix is full.

Filtering in the spectral algorithm is sometimes necessary to allow the wave computation to proceed longer in time when breaking occurs. The following filter is used:

$$f_i = \begin{cases} 1, & 1 \leqslant i \leqslant n_f \\ e^{-c_f(i-n_f)^2}, & n_f + 1 \leqslant i \leqslant N/2, \end{cases} \tag{3.12}$$

where f_i multiplies both Fourier coefficients with wavenumber i for all x, y, ϕ and ψ. When a filter is applied, we typically use c_f=1 and n_f=28 for N=64. This is a smooth low-pass filter that affects only a few high-frequency coefficients.

4. Typical computational results

4.1. *Convergence and stability*

The convergence of the spectral method is compared to the piecewise-linear method in Huh (1991) for steady test problems. Here, we briefly extend this comparison to time-marching by examining a gravity-wave problem with an initial amplitude of $a = 0.2$ in (2.4) for time $0 \leqslant t \leqslant 10$. Table 1 compares maximum errors (over $0 \leqslant t \leqslant 10$) in conservation of energy for varying N. The conservation of mass results are very similar. The conservation of energy is determined by $E_e = [E(t) - E(0)]/E(0)$, where E is given in the usual way by

$$E = \frac{1}{4\pi} \int y^2 \mathrm{d}x + \frac{1}{4\pi} \int \phi \mathrm{d}\psi. \tag{4.1}$$

The first and second terms represent potential and kinetic energy per unit surface area (V and T), respectively, and the integrals are along the free surface for one wavelength. The spectral computations results are not only much more accurate than the piecewise-linear technique (Huh 1991), but they are less computationally intensive. CPU times are listed for an Apollo DN-10000 RISC workstation for the strong algebraic system and varying error criteria ($\epsilon_t = \epsilon_c$) for the time-marching and iterative algebraic solver–LSODA and GMRES, respectively. All these computations for $a = 0.2$ can be computed indefinitely without further loss in accuracy (as tested to $t = 200$). The computations can fail if too high precision is required for low spatial resolution ($N = 16$) or if the required precision is close to machine precision ($N = 32$). Generally, much more accurate time marching is required to obtain the benefit of larger-N computations. For this initial condition, the spectral computations can give essentially double-precision (16 digit) machine accuracy when $N = 32$ and $\epsilon_t = \epsilon_c = 10^{-13}$.

4.2. *Steadily progressing waves*

We first show that under special circumstances waves of large amplitude do not necessarily break. Specifically, we examine gravity waves of permanent form, and suppress the Benjamin–Feir instability by applying periodic boundary conditions that do not allow subharmonic disturbances (Longuet-Higgins 1978). The initial conditions for a steadily progressing wave can be computed from a series expansion as performed by Stokes (1880) and extended using computer algebra by Schwartz (1974). Rather than use series acceleration techniques, we compute the initial conditions for our time-marching code from the iterative method of Schwartz & Vanden-Broeck (1979). We set their surface tension parameter to zero and modify their mapping slightly to desingularize the mapping at high amplitudes. Because obtaining accurate initial conditions is the 'weak link' in these computations, we compute twice as many points

N	$\epsilon_t = \epsilon_c$	max. E_e	CPU (s)
16	10^{-4}	2.6×10^{-3}	0.64
16	10^{-6}	5.2×10^{-5}	0.92
16	10^{-8}	3.4×10^{-7}	1.41
16	10^{-10}	failed	—
32	10^{-8}	1.0×10^{-7}	3.94
32	10^{-10}	1.5×10^{-9}	5.95
32	10^{-12}	1.3×10^{-11}	8.82
32	10^{-13}	8.1×10^{-13}	10.26
32	10^{-14}	failed	—
64	10^{-12}	1.8×10^{-11}	32.9
64	10^{-13}	1.6×10^{-13}	60.0

TABLE 1. Spectral computational comparison

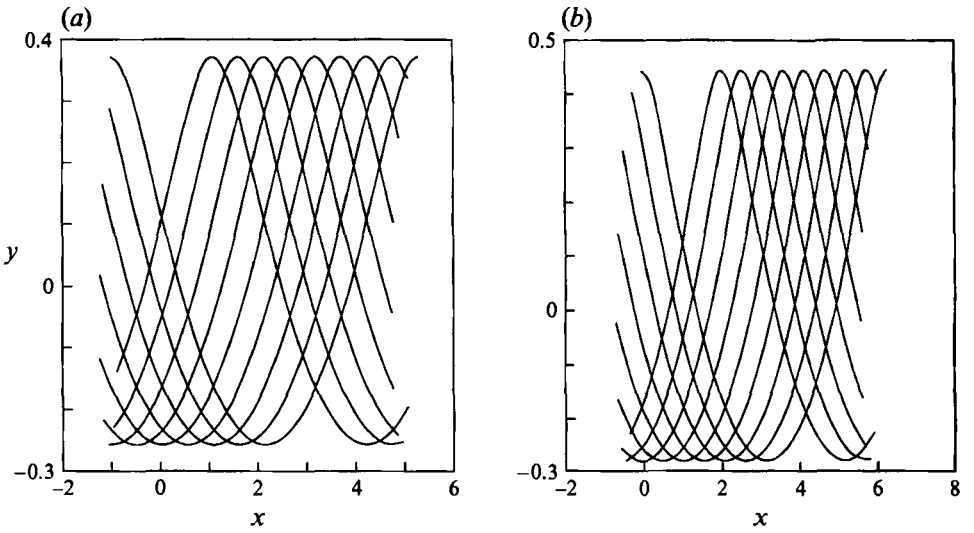

FIGURE 2. Steadily progressing wave profiles: (a) $(y_{max} - y_{min})/2\pi = 0.1$ (spectral), (b) $(y_{max} - y_{min})/2\pi = 0.115$ (piecewise-linear).

as we use in the time-marching algorithm and discard every other value. To obtain an accurate Jacobian matrix for proper convergence, these computations must be performed in double precision (16 digits). Surprisingly, unless the amplitude is near the limiting Stokes wave height that forms the 120° crest, single precision is sufficient for the time-marching algorithm.

Figure 2(a, b) shows eight wave height profiles spaced $\Delta t = 0.5$ apart for the amplitude parameter $(y_{max} - y_{min})/2\pi = 0.1$ and 0.115, respectively. Note that the vertical scale is greatly exaggerated in this figure and in all wave profiles to follow. The time-marching computations were performed using $N = 64$. The spectral algorithm was used in figure 2(a) while the more robust piecewise-linear algorithm was required for the computations of figure 2(b) since the amplitude is near the Stokes limit of $(y_{max} - y_{min})/2\pi \approx 0.14$. In any case, the conservation of energy criteria cannot be satisfied better than $E_e = 10^{-5}$ for long times using $N = 64$. The phase velocities

(as determined by marching for long time) are approximately 5.2 and 6.7 % higher than linear waves for the cases in figures 2(*a*) and 2(*b*), respectively and have converged to an accuracy of 0.005 %. The RMS variation in the peak-to-peak wave height is 8×10^{-5} for figure 2(*a*) and 2×10^{-4} for figure 2(*b*). The overdetermined system in this case is twice as accurate as the strong system and only requires 20 % more CPU time. The spectral computation was again the most accurate, conserving energy and mass to within one part in 10^9 (compared to one part in 10^4 for the equivalent piecewise-linear computations and one part in 10^3 for the higher wave of figure 2*b*). The potential energy V and kinetic energy T were constant to seven significant digits ($V = 0.02292022$, $T = 0.02412471$) for the computations shown in figure 2(*a*) and four significant digits for figure 2(*b*) ($V = 0.02903$, $T = 0.03110$). These waves are not found experimentally because they are subject to a Benjamin–Feir instability (that is suppressed here by the imposed periodic boundary conditions).

4.3. *Simple harmonic linear wave initial conditions*

Figure 3(*a*, *b*) shows typical computations of free surface profiles spaced $\Delta t = 0.2$ apart for two different initial amplitudes. The first family of curves for initial amplitude $a = 0.3$ results in a spilling breaker as shown in figure 3(*a*). When more energetic initial conditions are used, as in figure 3(*b*) ($a = 0.544$), the wave becomes a plunging breaker. The computation in figure 3(*a*) is within graphical accuracy to the piecewise-linear Cauchy integral and Green's function algorithm in McIver & Peregrine (1981). The spectral algorithm starts to break down as the algebraic system becomes ill-conditioned in the sense that the iterative solver can no longer drive the residual below the prescribed criterion ϵ_t. The wave profiles change from solid to dashed lines at this time. Until this time, the spectral (solid line) and piecewise-linear (dashed line) computations are nearly identical although the spectral result is far more accurate. The source of the breakdown is very steep gradients of $\mathrm{d}\beta/\mathrm{d}z$ near the nodes marked by circles in the last accurate wave profiles in figures 3(*a*, *b*). The computations can be made to proceed further in time by using an iterative procedure that simply minimizes the residual, but at the expense of being as inaccurate as the piecewise-linear computations. We are continuing to study this in an attempt to see if singularities develop in the inviscid model before 'breaking' occurs, as in the study of singularity formation in vortex sheets (Krasny 1986). Our experiences with filtering, changing the precision, adding extra constraints to make the algebraic system nonsingular, and using an overdetermined algebraic system show that the computations are affected only near breaking (Huh 1991). None of these techniques appear to allow accurate computations near breaking. This is consistent with the formation of a singularity. It would seem that surface tension, or regularization by adding dissipation is necessary to continue fully converged solutions further in time in a breaking simulation.

We have run numerical simulations for many values of a to determine the initial conditions (2.4) that cause breaking or spilling. We find that waves will spill for a slightly larger than 0.27 but will progress indefinitely for $a < 0.26$. Typical computations use $N = 60$ or 80 and $\Delta t = 0.1$ or 0.05. These results are somewhat sensitive to the initial conditions in that using a three-term Stokes wave height initial condition,

$$y = a \sin x + \tfrac{1}{2}a^2 \sin 2x + \tfrac{3}{8}a^3 \sin 3x, \tag{4.2}$$

does not apply as large a perturbation to the steady form, and, hence, the breaking

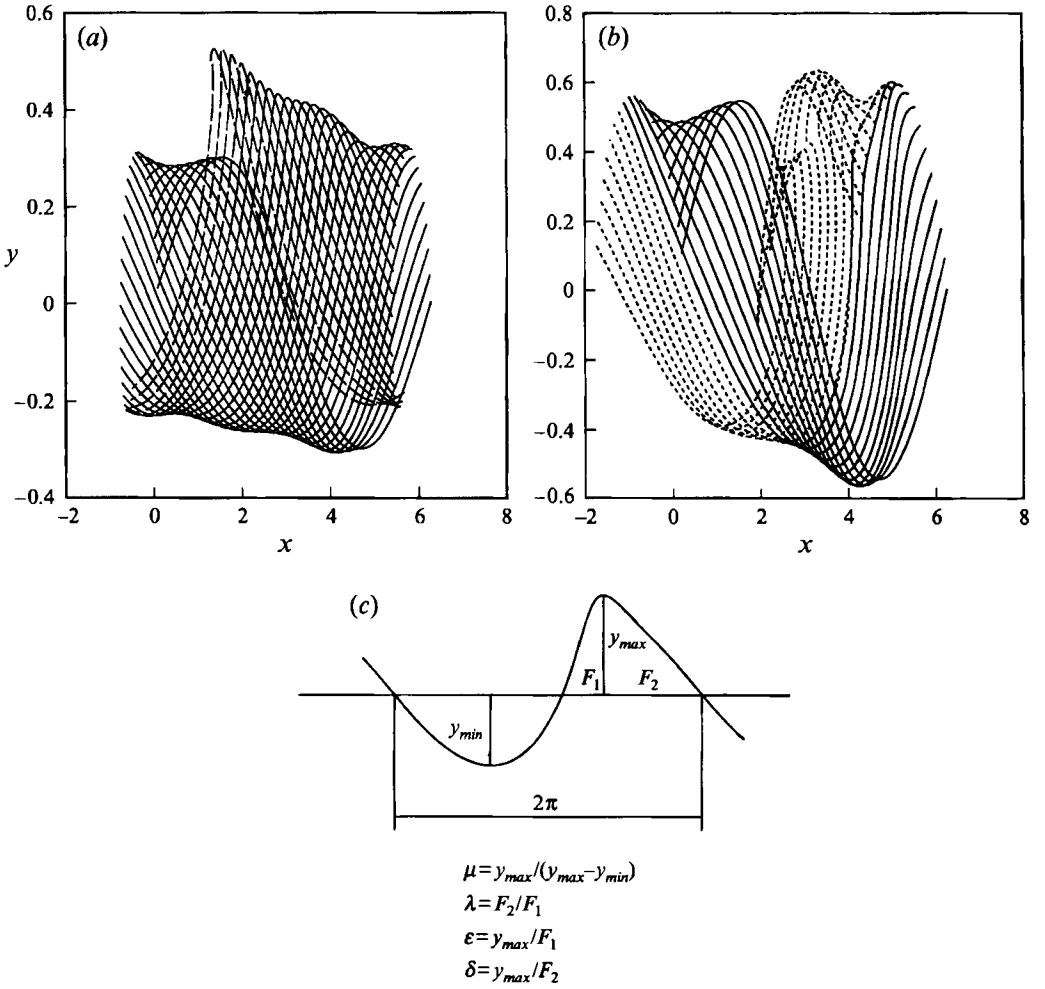

FIGURE 3. Free surface profiles ($\Delta t = 0.2$, $N = 64$): (*a*) spilling breaker ($a = 0.3$), (*b*) plunging breaker ($a = 0.544$), (*c*) breaking parameters (redrawn from Bonmarin 1989).

is suppressed to slightly higher amplitudes. This can be seen by examining the limiting case of an 'exact' steady waveform in figure 2(*b*), where $y_{max} - y_{min} = 0.722$ is maintained without breaking. However, a small subharmonic disturbance would cause these high waves to break.

The geometric properties are compared to Bonmarin's (1989) experiment for spilling breakers. The degree of asymmetry of the crest is expressed by horizontal and vertical asymmetry factors (μ and λ), and the steepness is expressed at the front and rear (ϵ and δ as defined in figure 3*c*). Our spilling results starting with simple harmonic waves agree with Bonmarin's experiment, as shown in table 2. The plunging wave comparisons are not as close, since the profiles (a=0.544) are close to vertical and give large values of λ and ϵ.

Since the total energy is constant throughout an entire numerical simulation as well as a (presumably inviscid) experiment, it would appear to be an ideal criterion to determine breaking. Unfortunately, without a carefully calibrated and instrumented wavemaker or the ability to measure the velocity everywhere in the flow field, the

		μ	λ	ϵ	δ
Bonmarin (1989)	Range	0.59–0.91	0.78–2.37	0.24–0.68	0.19–0.42
	Mean Value	0.75	1.38	0.41	0.31
Present results	a=0.3	0.72	1.93	0.62	0.32
	a=0.28	0.70	1.12	0.40	0.36

TABLE 2. Geometric properties of spilling breakers

total energy cannot be measured. Instead, a measured steepness criterion ($y_{max} - y_{min}$)/wavelength is usually used. We see from figure 4(a) that this criterion varies widely in time for the two cases with initial conditions (2.4) of $a = 0.27$ and 0.28. The non-breaking wave peak-to-peak height becomes higher than the value at a previous time for a wave that breaks. Hence, the height for a non-breaking wave could exceed that of a wave that is breaking. The computations show that the wave breaks at less than the maximum peak-to-peak height. There is experimental evidence for this as well (Melville & Rapp 1988).

However, the potential energy, although not constant in time, is roughly half of the conserved total energy. Hence, it is much less variable than the peak-to-peak values and still can easily be determined from wave probe data. Figure 4(b) demonstrates that the computed RMS wave heights (or potential energies) for these same two initial conditions are more distinct. That is, the RMS height of the breaking wave with initial condition $a = 0.28$ does not fall below the peaks of the non-breaking wave with initial condition $a = 0.27$, in contrast to the $y_{max} - y_{min}$ data. This indicates that potential energy may be a better criterion to determine whether a travelling wave will break. These computations also show that breaking does not occur at the peak of the potential energy. This can be anticipated since the increased fluid velocities near the crest would increase the kinetic energy at the expense of the potential energy. The potential energy at breaking is about 52 to 54% of the potential energy of the highest Stokes wave computed by Cokelet (1977). (These percentages would be approximately one percent higher when compared to the *limiting* Stokes wave, which has the 120° crest but is less energetic.) The *total* energy is 49 to 52% of that for the limiting Stokes wave, even though the kinetic energy is slightly more than the potential energy at the time of breaking. This energy is considerably lower than the computed wave with 2/3 the limiting wave energy predicted to break by Cokelet (1979).

It should be noted that the computational wave data are determined at the same instant of time for the results of figure 4(a), while experimental measurements using one wave probe are measured at one location for a temporal period.

Figure 4(a, b) also compares spectral and piecewise-linear computations. The piecewise-linear computations proceed further before breaking down, but as these computations are refined, they approach the spectral computations and do not fail earlier when more stringent error requirements are applied. Figure 4(c) shows the error in conservation of energy for several computations of the spilling breaker with initial amplitude $a = 0.30$ as shown in figure 3(a). All computations degrade with time such that an energy error of less than 10^{-5} is not possible at $T = 5.5$. For the cases that show a continual degradation of error, the time marching and residual error criteria (ϵ_t and ϵ_c) were made sufficiently strict such that the only error is that due to spatial discretization. The $N = 64$ and one of the $N = 32$ calculations showing a

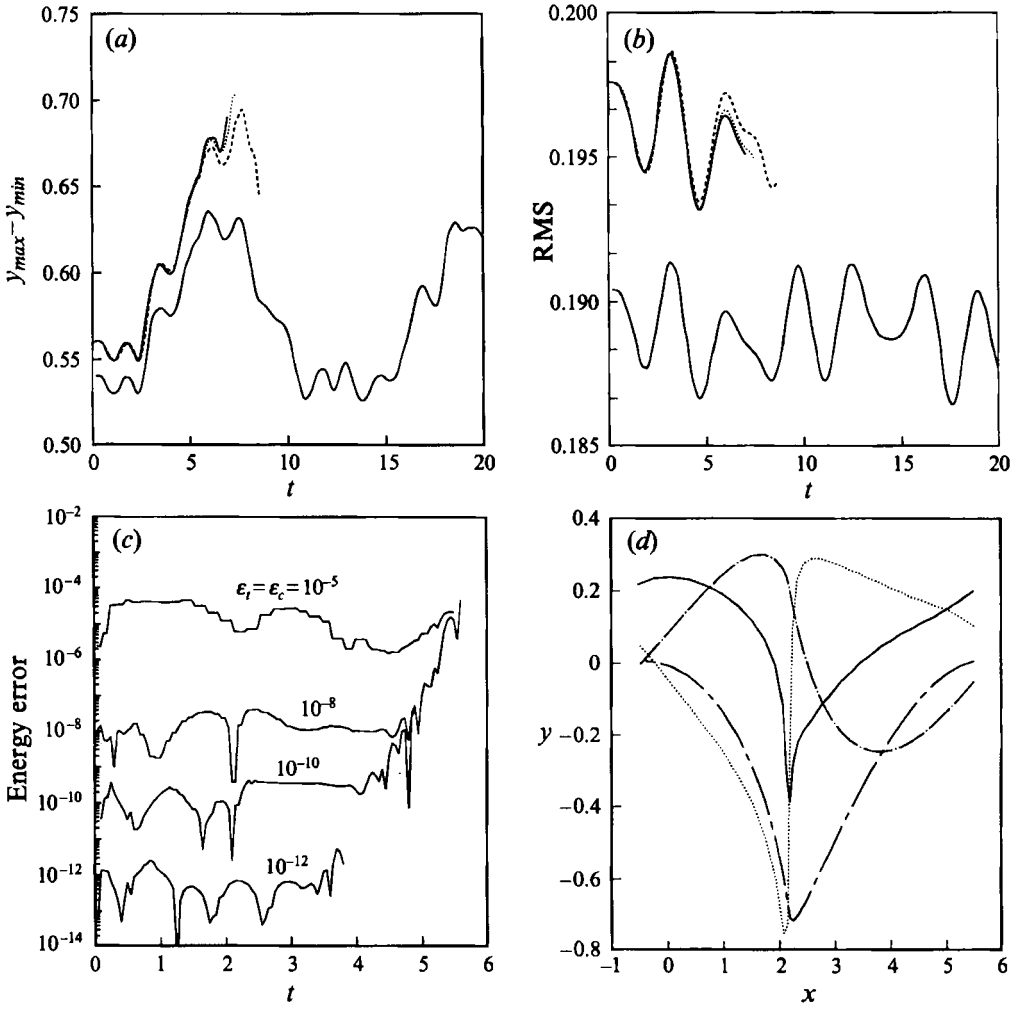

FIGURE 4. (*a*) Peak-to-peak wave heights for a =0.27 and 0.28: spectral $N = 32$, ————; piecewise-linear $N = 32$, — — —; piecewise-linear $n = 64$, ·····. (*b*) RMS wave heights for the same two initial conditions. (*c*) Energy conservation errors *vs.* time for spectral computations of a spilling wave ($a = 0.30$). (*d*) The formation of a possible singularity for a spilling wave ($a = 0.30$, $t = 5.0$, $N = 32$): ————, Real part $d\beta/dz$; — · — · —, Imaginary part $d\beta/dz$; — · — · —, vertical acceleration Dv/Dt; ·····, horizontal acceleration Du/Dt.

relatively constant error of 3×10^{-14} for $t < 3$ were limited by the above precisions. All the $N \geqslant 32$ spectral calculations are also limited by the double-precision arithmetic.

The solution appears to break down considerably before the Taylor instability mechanism (when the normal acceleration of the free surface exceeds the normal component of gravity) mentioned by Xü & Yue (1992) and others. This is shown in the potential derivatives and accelerations of figure 4(*d*) for the $a = 0.30$, $N = 32$ spectral computation. The figure shows very large changes near $x = 2$, in the location shown by the dots of figure 3(*a*). This indicates that it may be impossible to obtain solutions to a prescribed accuracy all the way until breaking. As an example, adding filtering and using an overdetermined system cannot yield a solution accurate to

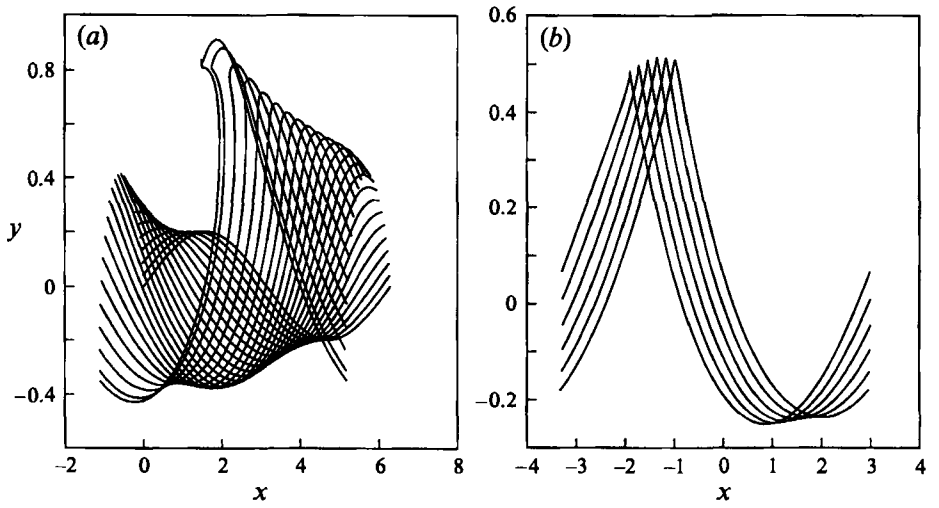

FIGURE 5. Wave profiles with exponential growth with increment between plotted profiles of $\Delta t = 0.2$: (*a*) rapid growth $\gamma = 0.5$, (*b*) slow growth $\gamma = 0.02$.

an energy error of less than 10^{-10} for this initial wave amplitude at a time $t = 5$. Again, this is consistent with the formation of a singularity in finite time. The spectral solutions using $N = 32$ and $N = 64$ are identical to graphical accuracy in figure 4(*d*) until $t = 5.0$. At that time, owing to the singularity, the high-frequency coefficients differ significantly depending on truncation. Plunging breaker simulations (not shown) show similar trends in computational accuracy. Filtering or use of a direct algebraic solver does not help the simulation progress further in time when simulating a breaking wave.

4.4. *Convergent wave channel*

The growth rate, γ, of equation (2.5) will cause any wave of any non-zero initial amplitude to break eventually. When the growth rate is large, the wave quickly plunges (figure 5*a*); when it is smaller, after a longer time the wave spills like those seen experimentally (figure 5*b*). The time required for the wave to break, of course, also depends on the energy and the details of the initial wave.

Figure 6 shows the temporal development of $y_{max} - y_{min}$, the potential energy, and the total energy for a growth parameter $\gamma = 0.2$ and two different initial conditions, $a = 0.1$ and $a = 0.2$. The average growth in the total energy for all cases is exponential at the rate expected, but with small oscillations. These oscillations are not computational errors, but artifacts of the growth model. The potential energy and the kinetic energy also grow exponentially but with larger oscillations. The lines of figure 6 cease at the time when the computation fails, which for these cases result in wave profiles that appear to be spilling breakers. All computations are spectral except for the dotted line, which shows small deviations of the peak-to-peak measurement near breaking for $a = 0.2$ when the piecewise-linear algorithm is used. In contrast to the no-growth breaking (figure 4*a*, *b*), these numerical simulations show breaking at or very near the maximum peak-to-peak wave height or potential energy. The wave grows to a higher value (by either measure) before breaking when the initial amplitude is smaller. This appears to be caused by the ability of the smaller wave to evolve in time more similarly to a nonlinear steadily progressive wave.

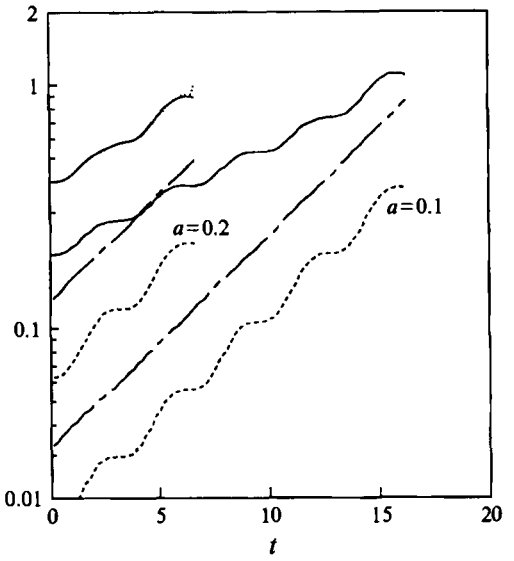

FIGURE 6. Evolution of wave diagnostics for spectral computations with growth parameter $\gamma = 0.2$ for two initial wave heights, $a = 0.1$ and 0.2: ————, $y_{max} - y_{min}$; — — —, V (potential energy); — - — - —, total energy; ·····, piecewise-linear results for $y_{max} - y_{min}$ for comparison.

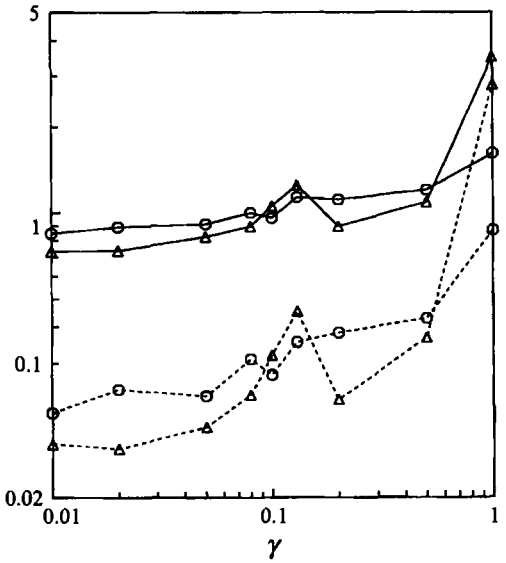

FIGURE 7. Breaking criteria for exponential growth conditions: o, $a = 0.1$; Δ, $a = 0.2$; ————, $y_{max} - y_{min}$; — — —, V, potential energy.

Breaking wave criteria for waves with varying growth rates can be obtained from figure 7. This shows that the breaking criteria (by either peak-to-peak or potential energy measures) increase with the energy input rate, except for a 'resonance' phenomenon around $\gamma = 0.1$, which appears to be an artifact of the periodic constraints.

The dependence of the breaking height has been correlated with growth rate by Van Dorn & Pazan (1975), who have also conducted experiments in a convergent channel. They obtain somewhat higher values of breaking wave height than those of Ramberg & Griffin (1987), which is consistent with the higher convergence rate of their channel ($\eta = 1/10$) compared to that for Ramberg & Griffin ($\eta = 1/16$).

4.5. *Modelling periodic submerged disturbances*

We examine the effect of underwater disturbances on the free surface, especially as it leads to wave breaking. For computational simplicity our two-dimensional potential flow algorithm uses a periodic dipole array to allow periodic boundary conditions. Duncan (1981, 1983) towed hydrofoils to create breaking waves while avoiding separation (which cannot be modelled in our potential flow model) and to create lift (which we prefer not to model since vortices are more difficult to model than dipoles). We 'tow' the dipole array at different speeds, depths, and dipole strengths (the radius of the approximate cylinder).

We tow the dipole at constant speed starting from rest with homogeneous initial conditions. From steady linear theory, the number of waves that should appear in a computational (or dipole array) period is equal to $1/v_{dp}^2$ (for our scaling). Here we have chosen v_{dp} values of -1 and -0.5 to represent 1- and 4-wave computations.

Figure 8(a, b) shows typical computations for a dipole starting at (2π, $-d_{dp}$) with unit depth, when $r_{dp} = 0.2$ and $v_{dp} = -1$. Figure 8(a) shows the initial development of the free surface (t=0, 1, 2, 3, 4) and figure 8(b) shows the last six profiles (t=28, 29, 30, 31, 32, 32.28) before the iterative procedure breaks down and a plunging breaker is formed. The free surface development is predicted with the same conditions except v_{dp}=-0.5 in figure 8(c) (t=0, 1, 2, 3, 4), and figure 8(d) (t=33, 34, 35). Initially, for both dipole speeds, a single peak occurs slightly ahead of the dipole, and a single trough occurs behind the dipole, as shown in figure 8(a, c). When v_{dp} is not -1, other peaks are observed as shown in figure 8(d), eventually forming the four local maxima when v_{dp}=-0.5, as predicted by steady linear theory. The conditions in figure 8(d) are close to those for a non-breaking wave, and hence, a small curling or 'spilling' breaker is formed rather than the plunging breaker of the previous case.

The peak-to-peak wave height ($y_{max} - y_{min}$) and RMS wave height are shown in figure 9(a, b) for various dipole strengths with $d_{dp} = 1$ and $v_{dp} = -1$, and in figure 9(c, d) for various dipole depths with $r_{dp} = 0.2$ and $v_{dp} = -1$. These numerical simulations show a temporal beating with breaking at or near the maximum values of the peak-to-peak wave height or potential energy. A nearly flat free surface can recur. The values of $y_{max} - y_{min}$ are more noisy than that for V — at least in part due to the sudden start of the disturbances. The waves begin to break close to the Stokes limit of $y_{max} - y_{min} = 0.88$. Similar behaviours are obtained when $v_{dp} = -0.5$, except under this condition the Stokes limit of wave height is approximately 0.22 (since four waves are generated in the 2π computational wavelength). The breaking occurs at the peak of the first beat period for $r_{dp} = 0.14$ (t=60), at the second for r_{dp}=0.12 (t=241.5) and at the third for r_{dp}=0.11 (t=420.6) as shown in figure 9(a, b). When r_{dp} is fixed and the depth is varied, waves break at the first peak for $d_{dp} = 1.8$ (t=65.2), at the second for d_{dp}=1.9 (t=213) and at the third for d_{dp}=2.0 (t=386) as shown in figure 9(c, d). For smaller radii and deeper depths, the breaking is not observed. Table 3 shows the minimum values of r_{dp} that cause breaking, $y_{max} - y_{min}$, RMS wave height, and beat period before breaking occurs for three combinations of dipole depth (0.5, 1, 2) and two speeds (-1, -0.5). The peak-to-peak and RMS wave heights at breaking when $v_{dp} = -0.5$ are similar to the previous cases such as

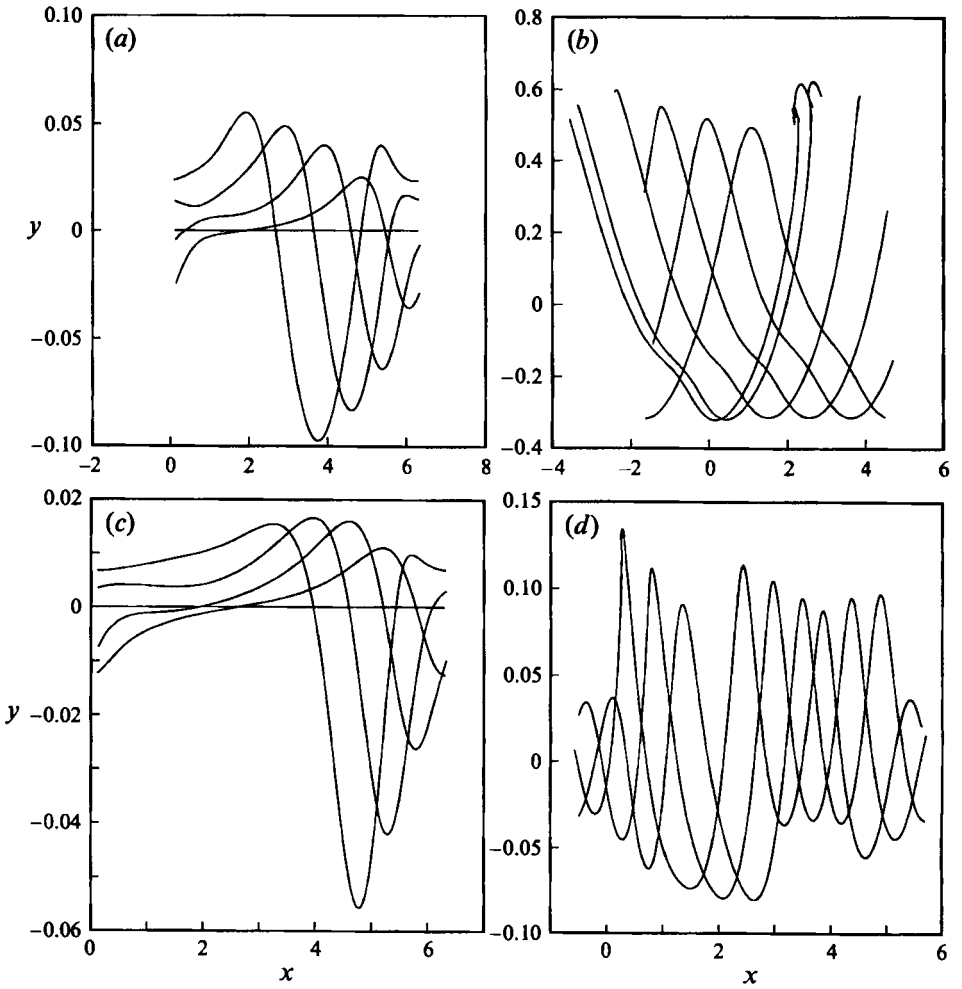

FIGURE 8. Wave profiles caused by a moving dipole: (*a*) initial development $v_{dp} = -1$, $r_{dp} = 0.2$, $d_{dp} = 1$, $0 \leqslant t \leqslant 4$; (*b*) final development $v_{dp} = -1$, $r_{dp} = 0.2$, $d_{dp} = 1$, $28 \leqslant t \leqslant 32.28$; (*c*) initial development $v_{dp} = -0.5$, $r_{dp} = 0.2$, $d_{dp} = 1$, $0 \leqslant t \leqslant 4$; (*d*) final development $v_{dp} = -0.5$, $r_{dp} = 0.2$, $d_{dp} = 1$, $33 \leqslant t \leqslant 35$.

in figure 4(*a*, *b*), especially for deeper dipoles. The $y_{max} - y_{min}$ values for $v_{dp} = -0.5$ are similar when multiplied by four, the number of wavelengths in the computational domain. However, the RMS heights for $v_{dp} = -0.5$ are underestimated since they are measured over the entire computational domain and are strongly affected by the non-breaking waves in multiple peak simulations.

While the potential energy representation is the same for the dipole-forced waves (except for the possible complication of multiple waves), the kinetic energy should exclude the kinetic energy inside the 'cylinder' formed by the dipole. Then, conservation of energy can be obtained by knowing the work done by the dipole using Lagally's theorem. We no longer check conservation of energy, but mass is still conserved to a high degree (the mean height error is typically 10^{-10} of the RMS wave height).

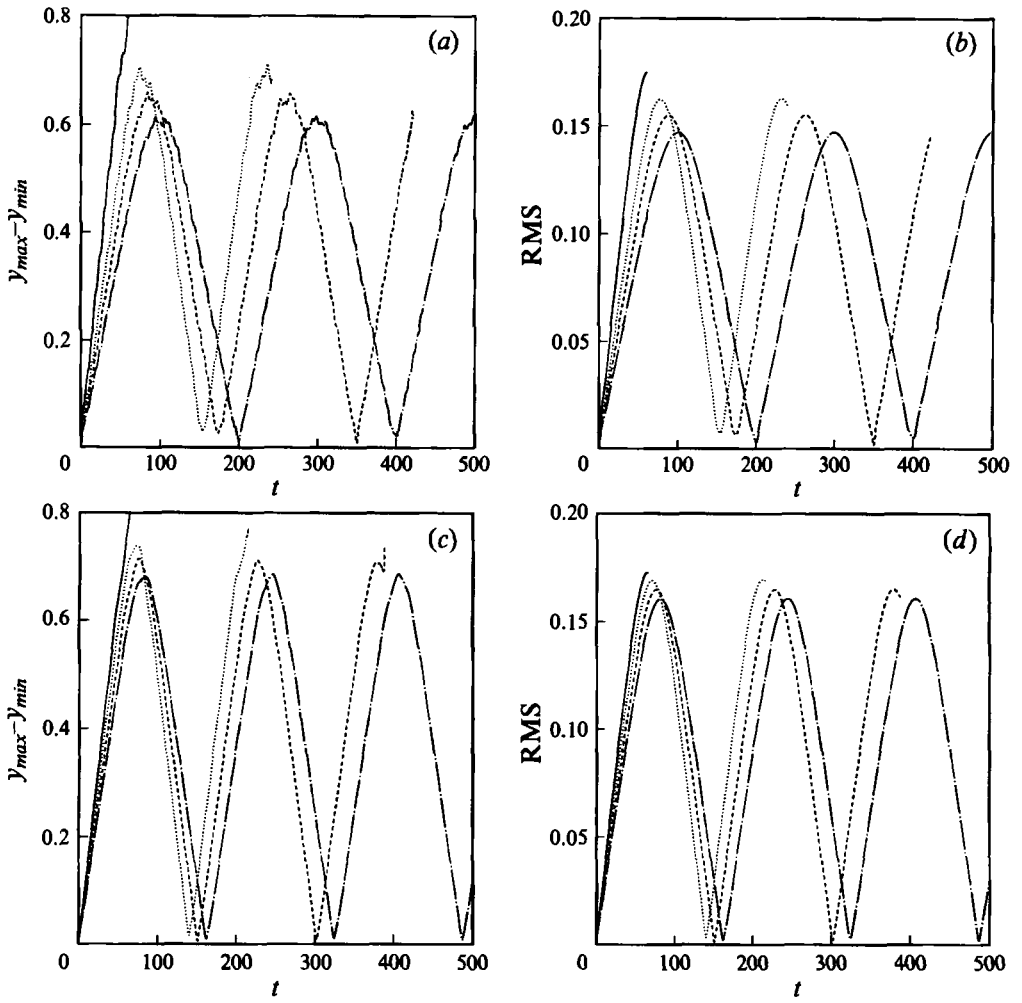

FIGURE 9. Computations of waves formed by moving dipoles. (*a*) $y_{max} - y_{min}$ and (*b*) RMS wave height for various r_{dp} ($v_{dp} = -1$, $d_{dp} = 1$): ———, $r_{dp} = 0.14$, $0 \leqslant t \leqslant 60$; · · · · · · · · ·, $r_{dp} = 0.12$, $0 \leqslant t \leqslant 241.5$; – – –, $r_{dp} = 0.11$, $0 \leqslant t \leqslant 420.6$; — · — · —, $r_{dp} = 0.1$, $0 \leqslant t \leqslant 500$. (*c*) $y_{max} - y_{min}$ and (*d*) RMS wave height for various d_{dp} ($v_{dp} = -1$, $r_{dp} = 0.2$): ———, $d_{dp} = 1.8$, $0 \leqslant t \leqslant 65.2$; · · · · · · · · ·, $d_{dp} = 1.9$, $0 \leqslant t \leqslant 213$; – – – –, $d_{dp} = 2$, $0 \leqslant t \leqslant 386$; — · — · —, $d_{dp} = 2.1$, $0 \leqslant t \leqslant 500$.

Our analysis can only be qualitatively compared to Duncan's experiments (1983) since they were affected both by the hydrofoil angle of attack and by the proximity of the hydrofoil to the channel floor (Duncan, personal communication). From figure 2 in his paper, we measure the wavelengths (42.62 cm, 41.5 cm, 38.33 cm) for three depths of submergence (21 cm, 19.3 cm, 18.5 cm), and compare to our analysis with four waves in the computational domain. These three dipole depths, speed (80 cm s^{-1}), and dipole radius (compare to the hydrofoil thickness of 2.54 cm) are scaled to $d_{dp} = 0.7739$, $v_{dp} = 0.4906$ and $r_{dp} = 0.0936$ for the first submergence (21 cm). Duncan's experiments showed a non-breaking wave when the depth is 21 cm, a transition from a non-breaking to a breaking wave when depth is 19.3 cm, and a breaking wave when depth is 18.5 cm. Figure 10(*a*, *b*) shows the peak-to-peak and RMS wave heights for these three dipole depths. Our computations show similar

d_{dp}	0.5		1.0		2.0	
v_{dp}	−1.0	−0.5	−1.0	−0.5	−1.0	−0.5
Min r_{dp}	0.06	0.04	0.11	0.07	0.2	0.37
$y_{max} - y_{min}$	0.51	0.16	0.62	0.14	0.70	0.17
RMS	0.13	0.021	0.14	0.015	0.16	0.021
Beat period	290	250	180	410	150	280

TABLE 3. Wave breaking caused by a periodic dipole array

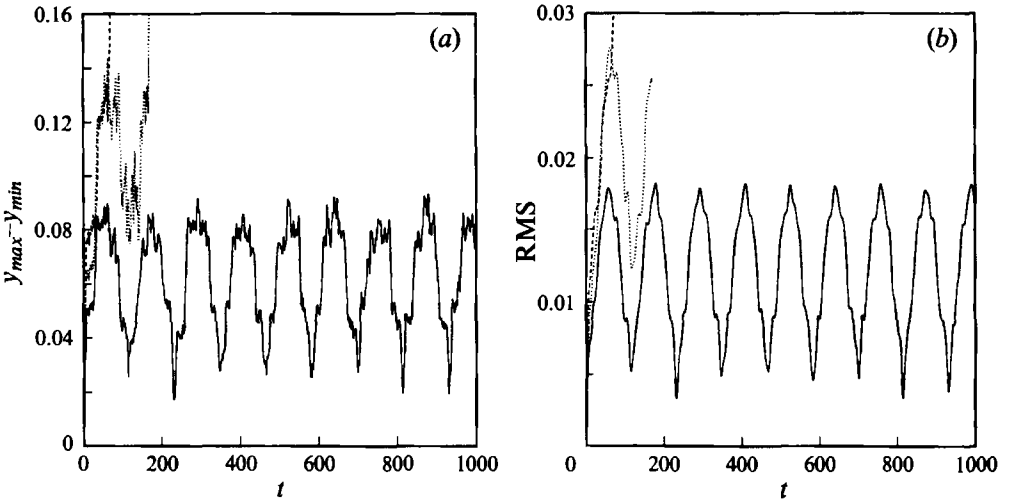

FIGURE 10. Wave computations for various dimensional dipole depths comparable to Duncan (1983) experiments: ————, depth = 21 cm; ·····, depth = 19.3 cm; – – – –, depth = 18.5 cm: (*a*) $y_{max} - y_{min}$, (*b*) RMS wave height.

behaviours as Duncan in that no breaking is observed when the dipole depth is 21 cm, the breaking occurs at the first peak (t=73.7) when depth is 18.5 cm, and at the second peak (t=167.9) when depth is 19.3 cm. However, the wave profiles are different since the angle of attack and bottom are missing from the model and the periodic dipoles affect the wave profiles. The large variances in wave behaviour for small variations in disturbance depth is, none the less, very striking.

4.6. *Wave modulation and reflection*

Experimental waves break at significantly less than the predicted Stokes limiting slope value, and even less than that predicted in the previous sections. For example in the convergent-channel data of §4.4, waves break at lesser heights presumably because of three-dimensional effects, viscous effects, wave reflections from beaches, and the Benjamin–Feir instability. We can easily test the last two effects on our two-dimensional algorithm. The modulational instability is modelled by taking a larger periodic domain and applying a subharmonic disturbance to the initial condition. Dold & Peregrine (1986) computed recurrence caused by modulation, but only briefly examined the effect of modulation on breaking waves. They showed a considerable decrease in the *average* breaking wave height as the modulation wavelength is increased. Figure 11 shows a limiting breaking wave from our spectral algorithm that

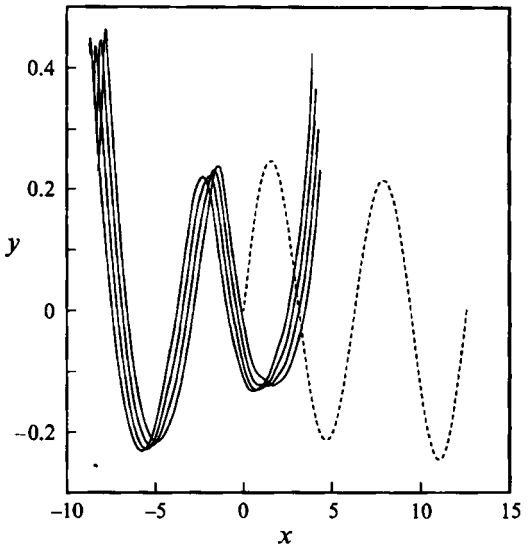

FIGURE 11. Breaking periodic wave with 10% initial modulation: – – –, initial wave profile ———, profile at breaking, $t = 97.0, 97.2, 97.4, 97.6$.

has a 10% modulation with a wavelength twice that of the primary wave. This is the easiest long-wave disturbance to model using a periodic algorithm and is the wavenumber that Longuet-Higgins (1978) found to be most unstable. The problem is now made 4π-periodic.

Specifically, the initial conditions we apply are those of (2.4) except that a is a 'slowly' varying function of x. For figure 11, $a = a'(1 + \beta \cos \frac{1}{2}x)$, where $a' = 0.23$ and $\beta = 0.10$. The initial wave profile is significantly to the left of the last three wave profiles before breaking because the long time to breaking ($t = 97.6$) allows for a significant amount of wave drifting. From this simple example, we see that a 10% modulation of the initial conditions causes an approximately 20% reduction in the initial size of a wave that breaks ($a = 0.28$ is reduced to 0.23). However, locally examining the wave at breaking yields $y_{max} - y_{min} = 0.64$ (using the average of the trough heights before and after the crest), within the scatter of the breaking criteria for unmodulated waves. This peak-to-peak criteria is 20% lower than the average of experimental waves (to be shown in § 5). However, the potential energy (as computed from the average of the last two waves) is 0.04, within 3% of the average potential energy for breaking wave experiments (also shown in § 5). This shows again that the potential energy is a better criterion for breaking than the wave slope. We are continuing to perform a more extensive computational study of modulated waves.

We also expect that reflection from the beach could cause smaller-amplitude waves to break. These reflections are modelled by applying the following free-surface initial conditions:

$$y = a\,(1 + \nu)\sin x \quad \text{and} \quad \phi = a\,(1 - \nu)\cos x, \tag{4.3}$$

where ν is the reflection coefficient, $\nu = 1$ corresponds to 100% reflection or standing waves. Figure 12 shows that, contrary to the the effect of modulation, a 10% reflection coefficient only modifies the initial conditions for breaking by approximately 5% ($a = 0.28$ is reduced to 0.265). The plots of $y_{max} - y_{min}$ and RMS are qualitatively similar to those of figure 4(a, b).

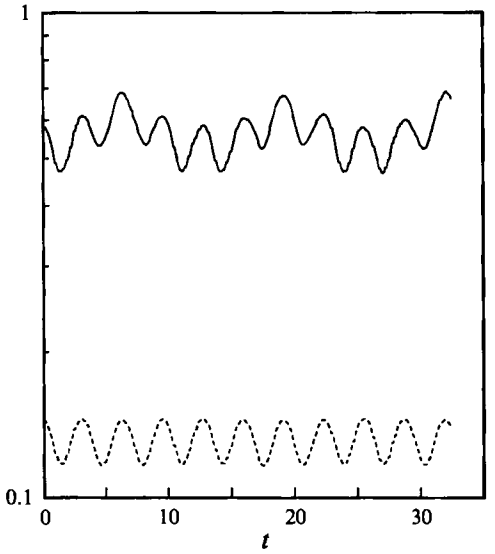

FIGURE 12. Breaking wave with reflection reflection coefficient is 10% with initial amplitude $a = 0.265$: ————, $y_{max} - y_{min}$; — — —, V, potential energy.

5. Comparison with convergent-channel experiments

The Naval Research Laboratory (NRL) experiments discussed in this section were conducted in a channel 30 m long and 1.3 m wide at the wavemaker with about 1.0 m mean water depth. The experimental procedures are described by Ramberg *et al.* (1985) and Ramberg & Griffin (1987). The channel was fitted with a convergent section with a rate of 1:16. This allowed the initially time-periodic waves (with prescribed frequency and amplitude) to grow into steep, asymmetric waves which often evolved into spilling and plunging breakers. Previous breaking wave experiments in a wave channel with a convergent section had been conducted and reported by Van Dorn & Pazan (1975).

Wave heights were measured with capacitance wave probes. The lengthscale for the experiments was $g(T/2\pi)^2$, such that the non-dimensional wavelength of a linear wave was 2π, in accordance with the periodic computations.

The location of wave breaking was established visually during the experiments as the position along the convergent channel where the sharp wave crests were first perceived to be 'tripping' into a spilling or plunging mode (where we first observed an increase in the crest fluid velocity over that of the travelling waveform). These locations were recorded and later compared to the positions where the measured variation of the average wave height $\bar{H}$ exhibited a transition from growth to attenuation along the channel. In all the cases compared, there was good agreement between these two estimated locations. Typical examples of spilling and plunging breakers are given in the photographs in Ramberg & Griffin (1987).

Two hundred equally spaced temporal measurements of wave height were taken over eight wavemaker periods with two probes placed 3.0 m apart. These measurements were repeated sequentially over twenty-four spatial locations.

It is often difficult to determine the breaking location, especially when breaking is intermittent. Figure 13 shows how the time spectra can help determine occurrences

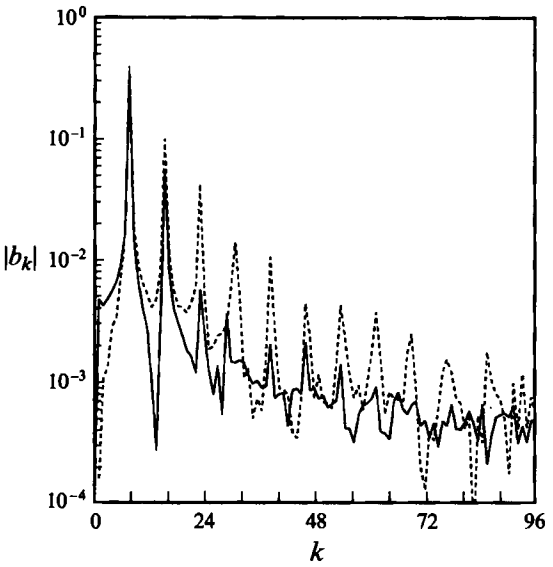

FIGURE 13. Fourier coefficients for wave data (experiments from Ramberg *et al.* 1985, 1987): – – –, breaking wave; ———, non-breaking wave.

of wave breaking. The complex representation is of wave height at one location

$$y = \sum_k b_k e^{ikt/8}, \tag{5.1}$$

where the 8 is in the denominator since data were taken during eight cycles of the wavemaker motion at each location. Figure 13 plots the magnitude $|b_k|$ *vs.* k for a breaking and non-breaking wave. Both have the same magnitude at the prominent peak at the primary frequency $k = 8$. When breaking occurs, the higher harmonics are much more pronounced. Also, the subharmonics are lower – indicating less wave modulation during breaking in these examples. This may be caused by the suppression of the highest waves by breaking. Although there is great variability in the spectra, breaking waves generally tend to have larger superharmonics and smaller subharmonics than comparable non-breaking waves.

At each location, for each wavemaker period, maximum and minimum wave heights were determined using quadratic interpolation. The mean and standard deviation of the non-dimensional peak-to-peak height, H, were determined for the eight cycles at each location. The potential energy of the experimental waves was computed by integrating the square of the height using Simpson's rule for six to eight full wave periods, as determined by consecutive crossings of the average datum height. After computing the mean potential energy, the standard deviation of potential energy between full wave periods was computed.

The average potential energy V values for all data (breaking and non-breaking) are shown in figure 14 as a function of the non-dimensional growth rate. The growth rate was determined from (7) even though some data were taken just into the non-convergent portion of the channel as described by Ramberg *et al.* (1985). Those waves determined to be at the point of incipient breaking are marked with closed symbols. The general trend of steeper breaking waves occurring for higher growth

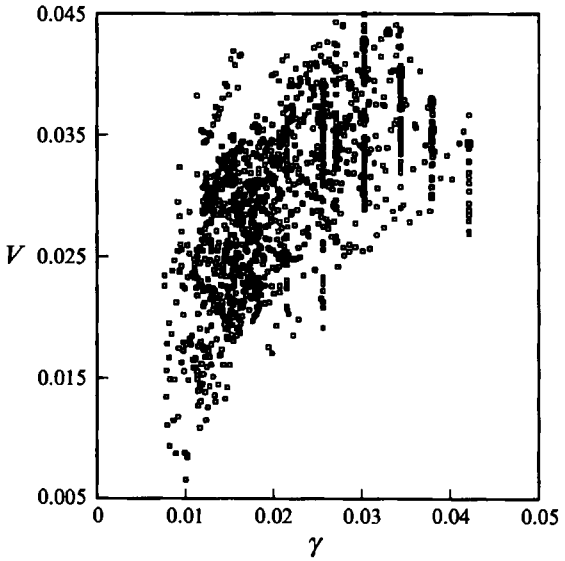

FIGURE 14. Potential energy for all data (experiments from Ramberg *et al.* 1985, 1987) (solid symbols denote incipient breaking waves).

rates is indicated by the larger breakers found further down the channel where the channel width is small.

A wide range of wave heights at the *onset of breaking* is shown in Schultz, Griffin & Ramberg (1987), Ramberg & Griffin (1987), and Bonmarin (1989) for recent investigations of deep water waves. The data from *all* of the experiments use a crest-to-preceding-trough value for H. The wave heights measured by Ochi & Tsai (1983) for the breaking of steep nonlinear waves in a uniform channel cover the range $gT^2 = 200$ to 800 cm, while the wave heights measured in the NRL experiments cover the range of $gT^2 = 550$ to 1100 cm. The wave heights measured by Duncan (1983) are between $gT^2 = 100$ and 400 cm and those measured by Bonmarin & Ramamonjiarisoa (1985) are between $gT^2 = 350$ and 650 cm. The latter experiments have recently been examined in more detail (Bonmarin 1989). These experiments were conducted to measure the unsteady breaking of waves in a uniform channel, while in the experiments of Duncan the steady breaking waves were generated by towing a hydrofoil through still water at various submergence depths. Above a critical submergence depth of the hydrofoil, wave breaking occurred spontaneously (Duncan 1983).

Schultz *et al.* (1987) and Ramberg & Griffin (1987) found that the dimensional peak-to-peak measurement of H for *breaking* waves was equal to a mean distribution with the wave period of $0.021gT^2$, corresponding to $H = 0.83$ in the present scaling as noted in figure 15(*a*). The Stokes steepness of $0.027gT^2$ represents an upper bound for all measurements of wave breaking (although unusual circumstances, such as high energy input, could cause steeper breaking conditions). This figure shows that H increases with the growth parameter γ, as predicted in figure 6. These predictions are higher than the experimental data – presumably owing to three-dimensional, viscous, and wave reflection and wave modulation effects in the experiments. The least-squares

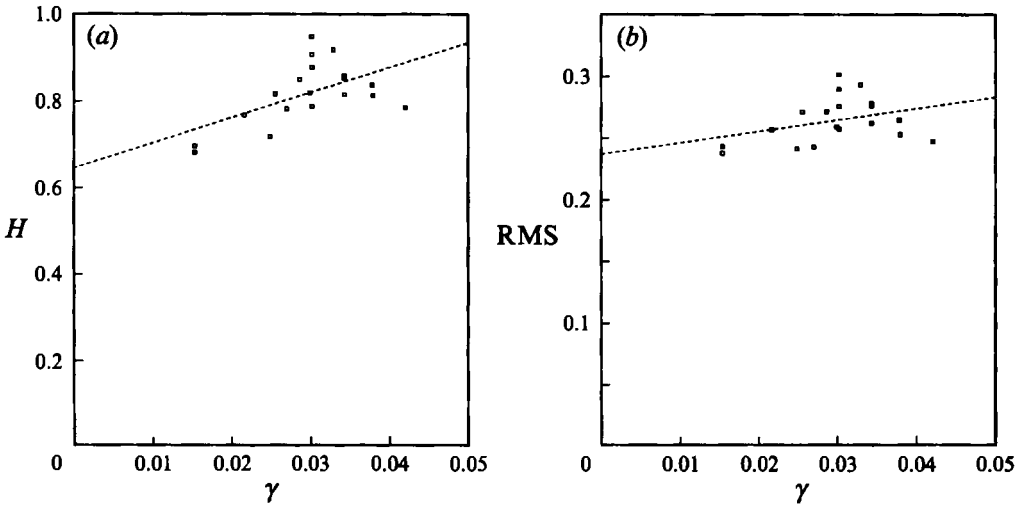

FIGURE 15. Breaking criteria applied to incipient breaking wave experiments from Ramberg *et al.* (1985, 1987): (*a*) peak-to-peak height, (*b*) RMS height.

linear fit of the breaking data in figure 15(*a*) is given by

$$H = 0.65 + 5.7\gamma\ . \tag{5.2}$$

The standard deviation about this curve is $\pm 7\,\%$ compared to $\pm 15\,\%$ peak-to-peak variation for the entire data set of figure 15(*a*).

The computations (e.g. figures 4*b*, 8*c*, 12) show that potential energy is 'better behaved' than the peak-to-peak (steepness) values. To check this for the experimental data, the corresponding V, or actually the RMS wave height, for breaking waves is shown in figure 15(*b*). A least-squares straight line fit for these data is

$$\text{RMS} = 0.237 + 0.89\gamma. \tag{5.3}$$

The RMS deviation from the linear fit is $\pm 6\,\%$. Hence, the RMS criterion for breaking is only marginally better than the peak-to-peak counterpart. The slope of the RMS curve fit is smaller, indicating that the RMS criterion is less sensitive to the growth rate. Also, the RMS wave height reduces scatter in the standard deviation of the measurement at one location. At each breaking event location, standard deviations of H and the RMS wave height for the six to eight cycles are calculated. The mean of these standard deviations is 3.2 % for $H = y_{max} - y_{min}$ and 2.7 % for the RMS height.

Comparisons of the experimental wave breaking location to the computations showed reasonable agreement (within 30 %) of the computed time of breaking multiplied by the group velocity, when a was chosen from linear wavemaker theory.

6. Comparison with wave packet breaking experiments

Recent experiments using focusing of wave packets (Peltzer, Griffin & Schultz 1994) are now analysed for comparison of breaking criteria. Rapp & Melville (1989), Bonmarin (1989) and Ochi & Tsai (1983) have also experimented extensively with breaking wave packets. Dommermuth *et al.* (1988) perform two-dimensional simulations of one event of a breaking wave packet with good comparison to experimental

	ϵ	RMS
Experimental mean	0.299	0.186
Experimental standard deviation (%)	13.8	7.6
Prediction	0.40	0.195
Predicted/experimental comparison (%)	25	5

TABLE 4. Properties of incipient breaking wave packets

results. Newer computations by Beck, Lao & Lee (1993) show nearly identical results using far less computer resources, but still too prohibitive to study many cases.

Table 4 shows the average of the crest front steepness ϵ (defined by Bonmarin 1989 and shown in figure 3*c*) and RMS of the average of the incipient breaking waves for the table 2 of Peltzer *et al.* (1994). We see that RMS is a more reliable and consistent criterion than a steepness criterion for breaking inception. The difference between the scatter of the two criteria for this example is significantly larger than the convergent-channel experiments. This is especially beneficial for the wave packet criterion because the RMS wave height can be predicted more directly and accurately than the wave steepness from simple group velocity considerations. Certainly, these are not spatially periodic waves and hence a criterion not based on wavelength is desirable — especially when the number of waves in a packet can change instantaneously. A potential energy per unit surface area criterion appears more consistent than a steepness criterion; however the potential energy or the RMS still uses a wavenumber (the local wavenumber measured at the breaking location for results in table 4) for non-dimensionalization. The refinement of the breaking criterion needs further study for this case.

7. Concluding remarks

Computations demonstrate that the potential energy of surface gravity waves is a better criterion for the onset of breaking for steep nonlinear waves than the wave slope. The computed wave height or steepness appears to have more erratic variations in time than the potential energy.

There are three experimental indications that the square root of the potential energy is better than the peak-to-peak wave height (or steepness) criterion in predicting the onset of breaking events. These are: (i) a better least-squares fit with wave channel location x, with half the scatter compared to that given by the peak-to-peak correlation, (ii) a smaller percentage standard deviation around the mean value at an individual location (breaking or non-breaking), and (iii) a smaller percentage variation of individual breaking events from an average breaking criterion.

Breaking criteria (peak-to-peak wave height or potential energy) depend on the energy input rate to the wave system, with the smallest values occurring when the *energy input rate* is small and spilling breakers are expected. A smooth transition to plunging breakers occurs (as conjectured by Longuet-Higgins & Cokelet 1976) for bigger waves that can be formed by a larger energy input rate. The dependence on the energy input rate further explains the scatter of breaking criteria derived from the convergent channel experiments. We have also found from experiments that breaking waves enhance the superharmonic and suppress the subharmonic frequencies.

Continuing studies show that the peak-to-peak wave heights and potential energy

that can be sustained without breaking are relatively independent of the method of wave formation. We find that the computations tend to show a higher breaking criterion (peak-to-peak wave height or potential energy) than that indicated by the experiments. This difference can be lessened by modelling the wave modulation and, to a lesser degree, wave reflection that are inherent in any experiment.

The work at The University of Michigan was supported by Naval Research Laboratory Contract No. N00014-85-K-2019, ONR Ocean Engineering Division Contract N00014-87-0509, and the Program in Ship Hydrodynamics at The University of Michigan, funded by the University Research Initiative of the Office of Naval Research, Contract No. N000184-86-K-0684. The work at the Naval Research Laboratory was conducted as part of an NRL basic research program in fluid dynamics. The authors wish to acknowledge many helpful discussions with S.E. Ramberg, R. Krasny, and J. Duncan. We acknowledge D.T. Rowley's contribution to the data reduction and L. Pall's editorial assistance.

REFERENCES

BAKER, G. R., MEIRON, D. I. & ORSZAG, S. A. 1982 Generalized vortex methods for free-surface flow problems. *J. Fluid Mech.* **123**, 477–501.

BANNER, M. L. & PEREGRINE, D. H. 1993 Wave breaking in deep water. *Ann. Rev. Fluid Mech.* **25**, 373–397.

BECK, R. F., CAO, Y. & LEE, T. 1993 Fully nonlinear water wave computations using the desingularized method. *6th Intl Conf. on Numerical Ship Hydrodynamics*, The University of Iowa.

BONMARIN, P. 1989 Geometric properties of deep-water breaking waves. *J. Fluid Mech.* **209**, 405–433.

BONMARIN, P. & RAMAMONJIARISOA, A. 1985 Deformation to breaking of deep water gravity waves. *Exp. Fluids* **3**, 11–16.

BOYD, J. P. 1989 *Fourier and Chebyshev Spectral Methods.* Springer.

CAO, Y., SCHULTZ, W. W. & BECK, R. F. 1990 Three-dimensional, unsteady computations of nonlinear waves caused by underwater disturbances. *18th ONR Symp. on Naval Hydrodynamics* (*Proc.*). National Academy Press, Washington DC.

COKELET, E. D. 1977 Steep gravity waves in water of arbitrary uniform depth. *Phil. Trans. R. Soc. Lond.* A **286**, 183–230.

COKELET, E. D. 1979 Breaking waves—The plunging jet and the interior flow-field. In *Mechanics of Wave–Induced forces on cylinders* (ed. T. L. Shaw). Pitman.

DOLD, J. W. & PEREGRINE, D. H. 1984 Steep unsteady water wave: An efficient computational scheme. *School of Mathematics University of Bristol Internal Rep.* AM–84–04.

DOLD, J. W. & PEREGRINE, D. H. 1986 Water-wave modulation. *School of Mathematics, Univ. of Bristol Rep.* AM–86–03, presented at *20th Intl Conf. on Coastal Engng, Taipei.*

DOMMERMUTH, D. G., YUE, D. K., LIN, W. M., RAPP, R. J., CHAN, E. S. & MELVILLE, W. K. 1988 Deep-water plunging breakers: a comparison between potential theory and experiments. *J. Fluid Mech.* **189**, 423–442.

DUNCAN, J. H. 1981 An experimental investigation of breaking waves produced by a towed hydrofoil. *Proc. R. Soc. Lond.* A **377**, 331–348.

DUNCAN, J. H. 1983 The breaking and non-breaking wave resistance of a two-dimensional hydrofoil. *J. Fluid Mech.* **126**, 507–520.

DUNCAN, J. H., WALLENDORF, L. A. & JOHNSON, B. 1987 An experimental investigation of the kinematics of breaking waves. *Rep.* EW–7–87, US Naval Academy.

HUANG, N. E., BLIVEN, L. F., LONG, S. R. & TUNG, C. C. 1986 An analytical model for oceanic whitecap coverage. *J. Phys. Oceanogr.* **16**, 1597–1604.

HUH, J. 1991 A numerical study of capillary–gravity waves. PhD thesis, University of Michigan.

KJELDSEN, S. P. & MYRHAUG, D. 1978 Kinematics and dynamics of breaking waves—Main report. *VHL Rep.*, Norway.

KRASNY, R. 1986 A study of singularity formation in a vortex sheet by the point-vortex approximation. *J. Fluid Mech.* **167**, 65–93.

LIN, W.-H., NEWMAN, J. N. & YUE, D. K. 1985 Nonlinear forced motions of floating bodies, *15th ONR Symp. on Naval Hydrodynamics* (*Proc.*), pp. 33–49. National Academy Press, Washington DC.

LONGUET-HIGGINS, M. S. 1978 The instabilities of gravity waves of finite amplitude in deep water: II. Subharmonics. *Proc. R. Soc. Lond.* A **360**, 489–505.

LONGUET-HIGGINS, M. S. 1981 A parametric flow for breaking waves. *Hydrodynamics in Ocean Engineering*, pp. 121–135. Norwegian Inst. Tech.

LONGUET-HIGGINS, M. S. 1985 Accelerations in steep gravity waves. *J. Phys. Oceanogr.* **15**, 1570–1579.

LONGUET-HIGGINS, M. S. & COKELET, E. D. 1976 The deformation of steep surface waves on water: I. A numerical method of computation. *Proc. R. Soc. Lond.* A **350**, 1–26.

MCIVER, P. & PEREGRINE, D. H. 1981 Comparison of numerical and analytical results for waves that are starting to break. *Intl Symp. on Hydrodynamics in Ocean Engineering*, pp. 203–215. Norwegian Inst. of Tech.

MELVILLE, W. K. 1982 The instability and breaking of deep-water waves. *J. Fluid Mech.* **115**, 165–185.

MELVILLE, W. K. & RAPP, R. J. 1985 Momentum flux in breaking waves. *Nature* **317**, 514–516.

MELVILLE, W. K. & RAPP, R. J. 1988 The surface velocity field in steep and breaking waves. *J. Fluid Mech.* **189**, 1–22.

OCHI, M. K. & TSAI, C.--H. 1983 Prediction and occurrence of breaking waves in deep water. *J. Phys. Oceanogr.* **13**, 2008–2019.

PELTZER, R. D., GRIFFIN, O. M. & SCHULTZ, W. W. 1994 Steepness and energy properties of deep water breaking wave packets. *Proc. Symp. on the Air–Sea Interface* (ed. M. Donelan), *Marseilles, June 1993*. Kluwer, in press.

RAMBERG, S. E., BARBER, M. E. & GRIFFIN, O. M. 1985 Laboratory studies of steep and breaking deep water waves in a convergent channel. *Naval Research Laboratory Memorandum Rep. 5610*. Washington, DC.

RAMBERG, S. E. & GRIFFIN, O. M. 1987 Laboratory studies of steep and breaking deep water waves. *Proc. ASCE, J. Waterways, Port, Coastal and Ocean Engng* **113**, 493–506.

RAPP, R. J., & MELVILLE, W. K. 1990 Laboratory measurements of deep-water breaking waves. *Phil. Trans. R. Soc. Lond.* A **331**, 735–800.

REED, A. M., BECK, R. F., GRIFFIN, O. M. & PELTZER, R. D. 1991 Hydrodynamics of remotely sensed surface ship wakes. *SNAME Trans.* **98**, 319–363.

ROBERTS, A. J. 1983 A stable and accurate numerical method to calculate the motion of a sharp interface between fluids. *IMA J. Appl. Maths* **31**, 13–35.

SAAD, Y. & SCHULTZ, M. H. 1986 GMRES: A generalized minimal residual algorithm for solving nonsymmetric linear systems. *SIAM J. Sci. Statist. Comput.* **7**, 856–869.

SCHULTZ, W. W., GRIFFIN, O. M. & RAMBERG, S. E. 1987 Steep and breaking deep water waves. *16th ONR Symp. on Naval Hydrodynamics* (*Proc.*), pp. 106–115. National Academy Press, Washington DC.

SCHULTZ, W. W. & HONG, S.-W. 1989 Solution of potential problems using an overdetermined complex boundary integral method. *J. Comput. Phys.* **84**, 414–440.

SCHWARTZ, L. W. 1974 Computer extension and analytic continuation of Stokes' expansion for gravity waves. *J. Fluid Mech.* **62**, 553–78.

SCHWARTZ, L. W. & VANDEN-BROECK, J.-M. 1979 Numerical solution of the exact equations for capillary-gravity waves. *J. Fluid Mech.* **95**, 119–139.

SROKOSZ, M. A. 1986 On the probability of wave breaking in deep water. *J. Phys. Oceanogr.* **16**, 382–385.

STOKES, G. G. 1880 Supplement to a paper on the theory of oscillatory waves. In *Mathematical and Physical Papers*, vol. 1, pp. 314–326.

VANDEN-BROECK, J.-M. 1980 Nonlinear stern waves. *J. Fluid Mech.* **96**, 603–611.

VAN DORN, W. G. & PAZAN, S. P. 1975 Laboratory investigation of wave breaking. II: Deep water waves. *Scripps Inst. Oceanog. Rep.* 75–21.

VINJE, T. & BREVIG, P. 1981 Numerical simulation of breaking waves. *Adv. Water Resources* **4**, 77–82.

XÜ, H. & YUE, D. K. 1993 Computations of fully-nonlinear three-dimensional water waves. *19th Symp. on Naval Hydrodynamics, Seoul, Korea.*